Correlating Microstructural Lithium Metal Growth with Electrolyte Salt Depletion in Lithium Batteries Using ^{7}Li MRI

Hee Jung Chang,[†] Andrew J. Ilott,[‡] Nicole M. Trease,[§] Mohaddese Mohammadi,[‡] Alexej Jerschow,[*,‡] and Clare P. Grey[*,†,§]

[†]Department of Chemistry, Stony Brook University, Stony Brook, New York 11794-3400, United States
[‡]Department of Chemistry, New York University, 100 Washington Square East, New York, New York 10003, United States
[§]Department of Chemistry, University of Cambridge, Lensfield Road, Cambridge CB2 1EW, U.K.

S *Supporting Information*

ABSTRACT: Lithium dendrite growth in lithium ion and lithium rechargeable batteries is associated with severe safety concerns. To overcome these problems, a fundamental understanding of the growth mechanism of dendrites under working conditions is needed. In this work, in situ ^{7}Li magnetic resonance (MRI) is performed on both the electrolyte and lithium metal electrodes in symmetric lithium cells, allowing the behavior of the electrolyte concentration gradient to be studied and correlated with the type and rate of microstructure growth on the Li metal electrode. For this purpose, chemical shift (CS) imaging of the metal electrodes is a particularly sensitive diagnostic method, enabling a clear

distinction to be made between different types of microstructural growth occurring at the electrode surface and the eventual dendrite growth between the electrodes. The CS imaging shows that mossy types of microstructure grow close to the surface of the anode from the beginning of charge in every cell studied, while dendritic growth is triggered much later. Simple metrics have been developed to interpret the MRI data sets and to compare results from a series of cells charged at different current densities. The results show that at high charge rates, there is a strong correlation between the onset time of dendrite growth and the local depletion of the electrolyte at the surface of the electrode observed both experimentally and predicted theoretical (via the Sand's time model). A separate mechanism of dendrite growth is observed at low currents, which is not governed by salt depletion in the bulk liquid electrolyte. The MRI approach presented here allows the rate and nature of a process that occurs in the solid electrode to be correlated with the concentrations of components in the electrolyte.
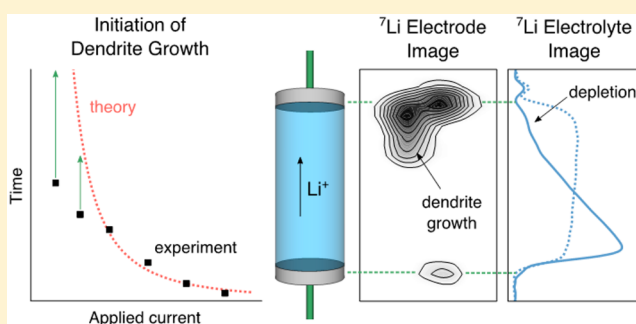
1. INTRODUCTION

The use of Li metal in rechargeable batteries is often accompanied by complications arising from morphological changes of the Li metal following continuous stripping and plating, leading to dendrite growth and severe safety issues.[1,2] Although much effort has been made to address the problems associated with dendrite growth,[3−9] fundamental studies are still required to better understand the chemistry occurring at the solid−solution interface under electrochemical potentials so that dendrite growth can be controlled or prevented.

There are various factors that potentially impact Li deposition morphology, such as the solid electrolyte interphase (SEI), battery components (electrodes, separators, and electrolytes), current density, stack pressure, electrolyte concentration gradient, and temperature. There have also been various models proposed to describe the conditions required for the onset and proliferation of dendrite growth in electrochemically grown metal systems. For example, the recent review by Li et al.[10] provides a thorough discussion of models relevant to dendrite growth in both lithium ion and lithium metal secondary

batteries. Of note are three models that can be classified by the factors that nominally contribute to the onset, growth rate, and morphology of metal deposition: (i) the Barton and Bockris model,[11,12] (ii) diffusion-limited Brownian models,[13,14] and (iii) electromigration-limited models developed by Chazalviel.[15] The Barton and Bockris[11] model, developed initially for Zn plating, proposes that dendrites grow preferentially from the tip of existing protrusions, where there is enhanced spherical diffusion as compared to the linear diffusion that occurs at the planar surface of the electrode. Both the threshold of initiation and the propagation of dendrite growth are determined from the critical overpotential at which the diffusion changes from linear to spherical. In the Brownian simulation model,[13,14] two parameters control the morphology of electrodeposition: the sticking coefficient, which refers to the deposition probability of a mobile cation to the metal surface, and the concentration of particles in the electrolyte solution. The model excludes any

physical parameters such as surface tension, reaction kinetics, or surface roughness, although these quantities are partly encapsulated in the value of the sticking coefficient.[4,16,17] When the deposition probability is low, there is an increased chance of forming dense structures, while a high deposition probability results in deposition at the tip of the existing protrusions, leading to dendritic structures.

The Chazalviel model[15,18] explores dendrite growth triggered by changes in the electrolyte concentration at the surface of the electrode. Two different behaviors in the ionic concentration gradient are predicted, at low and high current density. At low current density, the concentration gradient in the electrolyte reaches a steady state, resulting in a stationary ion distribution and potential in the cell, with no dendrite growth expected. In contrast, at high current density, a steady state is not reached, and the concentration continuously depletes in the vicinity of the negative electrode until eventually the anion concentration drops to zero after a certain amount of time, referred to as Sand's time.[15] The excess of positive charge violates charge neutrality, producing a large space charge and electric field at the electrode, resulting in the nucleation and unavoidable growth of dendrites. Sand's time depends on measurable properties of a cell, allowing it to be used to predict the onset time of dendrite growth. Methods that can directly measure dendrite growth in situ can thus provide a route to validate this model and gauge the importance of the changing ionic concentration in governing dendrite growth.

For a given cell geometry and composition, the Chazalviel model defines a critical current density, J^*, which marks the boundary between the low and high current behavior described above. J^* is determined by the initial electrolyte concentration (C_0), the ambipolar diffusion coefficient (D), and the distance between the electrodes (L), according to

$$J^* = \frac{2eC_0D}{t_aL} \tag{1}$$

where t_a is the transport number for the anion and e is the elementary positive charge. The time required for the anion concentration to drop to zero at the negative electrode for a given current density (J), termed Sand's time (τ_s), is also defined:

$$\tau_s = \pi D\left(\frac{C_0e}{2Jt_a}\right)^2 \tag{2}$$

Brissot et al. measured the ionic concentration map experimentally using optical microscopy on a symmetric Li cell with a PEO [poly(ethylene oxide)] polymer electrolyte in order to validate the Chazalviel model.[18] They demonstrated that the onset time of dendrite growth (also measured optically) at high current density is in good agreement with the predicted Sand's time. However, later observations showed clear evidence of dendrite growth, even at current densities below J^*.[18,19] It was proposed that the nonuniformity of the electrode surface can cause variations in the local current density in the vicinity of the electrode. Sand's time has also been shown to be inversely proportional to the temperature of the cell (using a Li symmetric cell with LiPF$_6$ electrolyte dissolved in a 1:1:1 volume ratio mixture of ethylene carbonate:dimethyl carbonate:ethyl methyl carbonate (EC:DMC:EMC)).[20] Plating of lithium metal in organic electrolytes is further complicated by the thick solid electrolyte interphase (SEI) layer that (i) affects Li$^+$ ion transport to the lithium metal surface and (ii) is highly heterogeneous, creating local current hot spots and presumably electrolyte concentration gradients. The flexibility of the SEI and its cohesion to the metal surface during Li deposition/stripping processes play important but poorly understood roles in controlling the growth of Li microstructures.[2,21−23] It is important to stress that the models discussed above were derived for electroplating of systems with no extensive passivation layer (although there have been extensions of the Brownian model to include an implicit SEI layer around the electrode surface).[4]

In situ nuclear magnetic resonance (NMR) spectroscopy and magnetic resonance imaging (MRI) are powerful tools that can provide time-resolved, quantitative information about battery materials and electrolytes. This has included in situ NMR measurements observing the growth of Li microstructures. Bhattacharyya et al.[24] showed the importance of considering the skin effect, whereby the radiofrequency (rf) field used to excite and detect the MR signal decays exponentially at the surface of a conductor with a characteristic length given by the skin depth constant, δ. In practice, this makes the MR spectra of conductors extremely sensitive to changes occurring on the length scale of δ, which is on the order of 10 μm for ^{7}Li at typical NMR fields. Two different Li resonances were observed in the metal region of the NMR spectra, the peak at 245 ppm corresponding to bulk Li metal and a peak at 270 ppm corresponding to microstructural Li deposits on the surface of the electrode, the shift difference being ascribed to bulk magnetic susceptibility (BMS) effects.[25−28] Smooth, uniform Li depositions on the metal surface are not detectable with NMR, as they do not result in an increase in the total volume that can be excited by the rf pulses when the thickness of the electrode is much greater than δ.[28] Combined with an understanding of these phenomena, NMR is a powerful tool for observing microstructural growth and correlating it with other properties of the cell, for example, pressure and separator effects[28] or changes in the electrolyte, with dendrite growth shown to be more efficiently suppressed in cells with an ionic liquid electrolyte in comparison to the standard 1 M LiPF$_6$.[3,24] A natural extension of the NMR approach has been to include spatial information using MRI. This technique has been demonstrated using chemical shift imaging (CSI) to reveal the location of different types of Li microstructures during the charge cycle of a Li metal symmetric cell.[29] The extra spatial resolution provided further confirmation of the peak assignment, revealing that the dendritic Li features have a narrow range of chemical shifts near 270 ppm, while mossy microstructures have broader peaks covering a large frequency range from 262 to 274 ppm. These assignments were further supported by a combination of SEM and NMR methods and simulation.[28]

Recently, in situ MRI approaches have been extended to the study of electrolyte concentration gradients in batteries.[30,31] Klett et al. reported one-dimensional (1D) ^{7}Li electrolyte concentration gradients in Li symmetrical cells containing 1 M LiPF$_6$ in EC:diethylene carbonate (DEC) mixed with 15 wt % poly(methyl methacrylate) (PMMA).[30] While applying currents in the range from 0.24 to 0.40 mA cm^{-2}, the evolution of the concentration gradient was observed. The electrolyte imaging profiles were used to quantitatively analyze physical constants of diffusivity and the Li$^+$ transport number within an electrochemical transport model.[32] Klamor et al. performed in situ ^{7}Li NMR imaging to study the formation of the SEI layer in a Li/nano-Si−graphite composite battery cycled at a constant

current of 0.07 mA cm^{-2}.[31] Local changes of ionic concentration at the interphase between electrode and electrolyte were observed, suggesting partial decomposition of electrolyte components during discharge. The above two studies provide detailed information about the evolution of concentration gradients in the electrolyte during cycling, but did not make any attempt to correlate these observations with changes occurring at the electrodes, such as those associated with Li deposition and microstructure formation.

Here we demonstrate a combined MRI study of the ^{7}Li electrolyte and ^{7}Li metal in symmetric Li metal cells charged in situ with a range of applied currents. This approach allows a direct correlation to be made between the growth of dendrites (and other types of dense microstructures, referred to as mossy structures in this study) with changes in the electrolyte concentration gradient. An analysis is performed to investigate the validity of Chazaviel's model and the accuracy of the theoretical Sand's time and to understand the impact of Sand's time on the dendrite growth in this system. We demonstrate that accurate estimates of the start time of dendrite growth can be obtained using chemical shift images of the ^{7}Li metal signal, which agree with theoretical Sand's time predictions at high current densities. At low currents, dendrites begin to grow more quickly than predicted, suggesting that other mechanisms are dominant in cells charged at low current densities.

2. EXPERIMENTAL SECTION

2.1. Sample Preparation. Electrochemical cells were prepared in a home-built cell fitted inside of a 15 mm glass tube and consisted of two electrodes of metallic lithium (diameter of 6.35 mm, Aldrich 99.9%) separated by an approximately 8 mm gap filled with electrolyte, the exact value varying slightly depending on the construction of the different cells used. The electrolyte used was 1 M LiPF$_6$ in 1:1 by volume EC:DMC (Novolyte). Following the approaches in the literature for similarly designed cell geometries,[30,31] 5% PMMA was also added to the electrolyte in order to increase its viscosity and thus reduce the impact of convection. All cells were prepared in an argon glovebox (O$_2$ and H$_2$O < 0.2 ppm), sealed with wax, and immediately transferred to the NMR magnet for imaging.

Electrochemical cycling was performed using a Biologic VSP potentiostat. Six different cells were prepared and each of them was charged at a constant current in one direction. Currents of 0.16, 0.32, 0.51, 0.76, 1.01, and 1.26 mA cm^{-2} were used. These currents were chosen to span either side of the calculated critical current density for the cell, $J^* = 0.58$ mA cm^{-2}. This value of J^* was calculated on the basis of eq 1, where $C_0 = 6.02 \times 10^{20}$ cm^{-3}, $L = 0.8$ cm, $D = 1.57 \times 10^{-6}$ cm^2 s^{-1}, and $t_a = 0.65$. This value for D is approximated as $2D_aD_c/(D_a + D_c)$ and calculated from the experimentally measured diffusion coefficients for the anion ($D_a = 2.26 \times 10^{-6}$ cm^2 s^{-1}) and the cation ($D_c = 1.20 \times 10^{-6}$ cm^2 s^{-1}), while t_a is approximated as $D_a/(D_a + D_c)$. The current was applied from the bottom electrode (positive electrode) to the top electrode (negative electrode). For this arrangement, Li deposition occurs at the top electrode (negative electrode), and Li stripping occurs at the bottom electrode (positive electrode).

2.2. Magnetic Resonance Imaging. All MRI and NMR experiments were performed on a Bruker Ultrashield 9.4 T Avance I spectrometer containing a Bruker Micro2.5 gradient assembly and operating at 155.51 MHz for ^{7}Li. A Bruker Micro2.5 imaging probe was used to collect all of the data, with a Bruker WB40 25 mm inside diameter ^{1}H/^{7}Li coil insert for the ^{7}Li experiments and a Bruker WB40 25 mm i.d. ^{1}H/^{19}F coil insert for the ^{19}F diffusion experiments.

The cells were aligned in the magnet such that B_0 (and the z-axis of the gradients) was aligned perpendicular to the face of the electrodes (as illustrated in Figure 1). The cells were centered in the coil, the excitation profile of which was found to be approximately 15 mm, thus ensuring uniform excitation over all of the components in the cell.
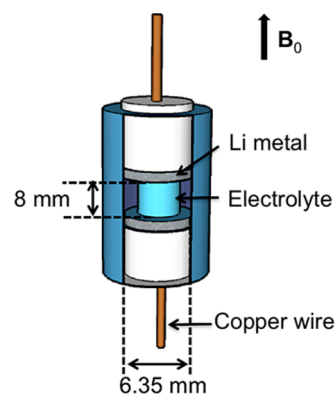

Figure 1. Schematic of the cell used for in situ MRI.

Imaging experiments could be performed separately on the ^{7}Li metal and electrolyte signals because of their significant chemical shift difference, arising from the 261 ppm Knight shift of ^{7}Li metal.[33,34]

Two types of images were collected during the cycling of the cells: a 1D ^{7}Li z-projection image of the electrolyte to give information on the concentration profile and a ^{7}Li metal chemical shift image (CSI) to observe changes in the bulk Li metal. Timing diagrams of both pulse sequences are given in Figure S1 of the Supporting Information (SI). The 1D ^{7}Li electrolyte image was acquired with a spin echo sequence in the z-direction, with a field of view (FOV) of 40 mm and a nominal resolution of ca. 16 μm. A total echo time (TE) of 3.5 ms was used with a repetition time (TR) of 8 s and 128 averages collected, giving a total experiment time of ca. 17 min. For the metal spin echo CSI, the chemical shift information was preserved during the readout while spatial encoding was performed with 32 phase increments in the z direction with a FOV of 30 mm and nominal resolution of 940 μm. With TR = 200 ms, TE = 0.65 ms, and 192 transient averages collected, the total experiment time was ca. 21 min. We note that although the spatial resolution in the metal CSI is not particularly high, it is sufficient to serve the purpose of separating the signal from each electrode in the cell while allowing images with high signal-to-noise ratio to be collected in a short amount of time, making the experiment amenable to in situ measurements.

The diffusion coefficients of the cation (Li$^+$, measured via ^{7}Li) and anion (PF$_6^-$, measured via ^{19}F) in the electrolyte were measured using a spin echo diffusion experiment with a fixed echo time. For ^{7}Li, the duration of the gradient pulse (δ) was 12 ms with a time interval between the gradient pulses (Δ) of 25 ms. For ^{19}F, δ = 4 ms and Δ = 20 ms. The measurements were taken on the electrolyte in the pristine cells prior to the in situ measurements, with gradient strengths stepping from 4 to 80 G cm^{-1} in the z-direction with 16 increments.

3. RESULTS AND DISCUSSION

Figure 2 shows examples of the ^{7}Li images acquired during the charge process of the cells, with the ^{7}Li electrolyte concentration profile (top) from the series of z-projection spin echo images and the chemical shift images of the ^{7}Li metal (bottom), from the cell charged at 0.78 mA cm^{-2} for 32.7 h. Before applying current, the lithium concentration profile at equilibrium shows a rectangular shape, associated with a uniform distribution of Li ions across the cell (Figure 2a). We observe that the salt concentration at the top electrode is slightly higher; this was also observed in the electrolyte profiles reported by Klett et al.[30] and is attributed to a slight variation in the radio frequency field of the coil over the z-axis. Some smearing occurs at the edges due to susceptibility effects near the surface of the Li metal,[25] the fact that the Li metal electrodes are not completely flat (as discussed below), and inhomogeneities in the rf field near the electrodes.[25,35,36] The associated CSI image of the pristine cell (Figure 2a, bottom)
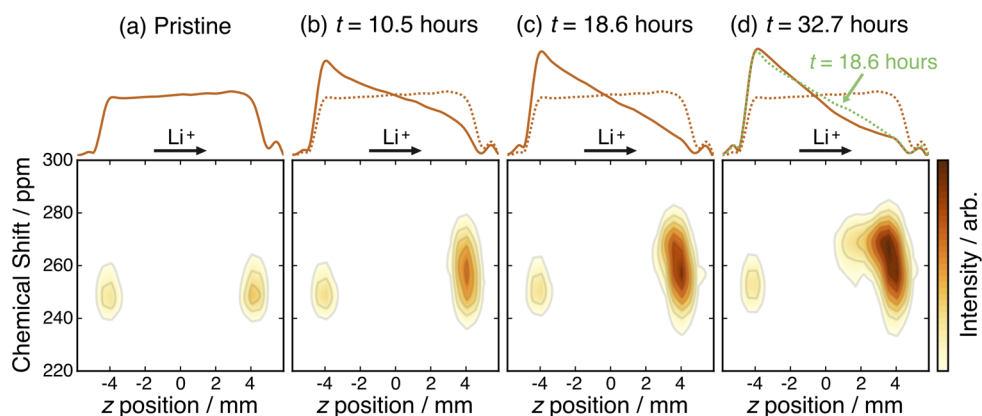
Figure 2. MRI time series showing the evolution of the ^{7}Li electrolyte concentration profile (top) and the ^{7}Li chemical shift image of the metal (bottom) for the cell charged at 0.76 mA cm^{-2}.
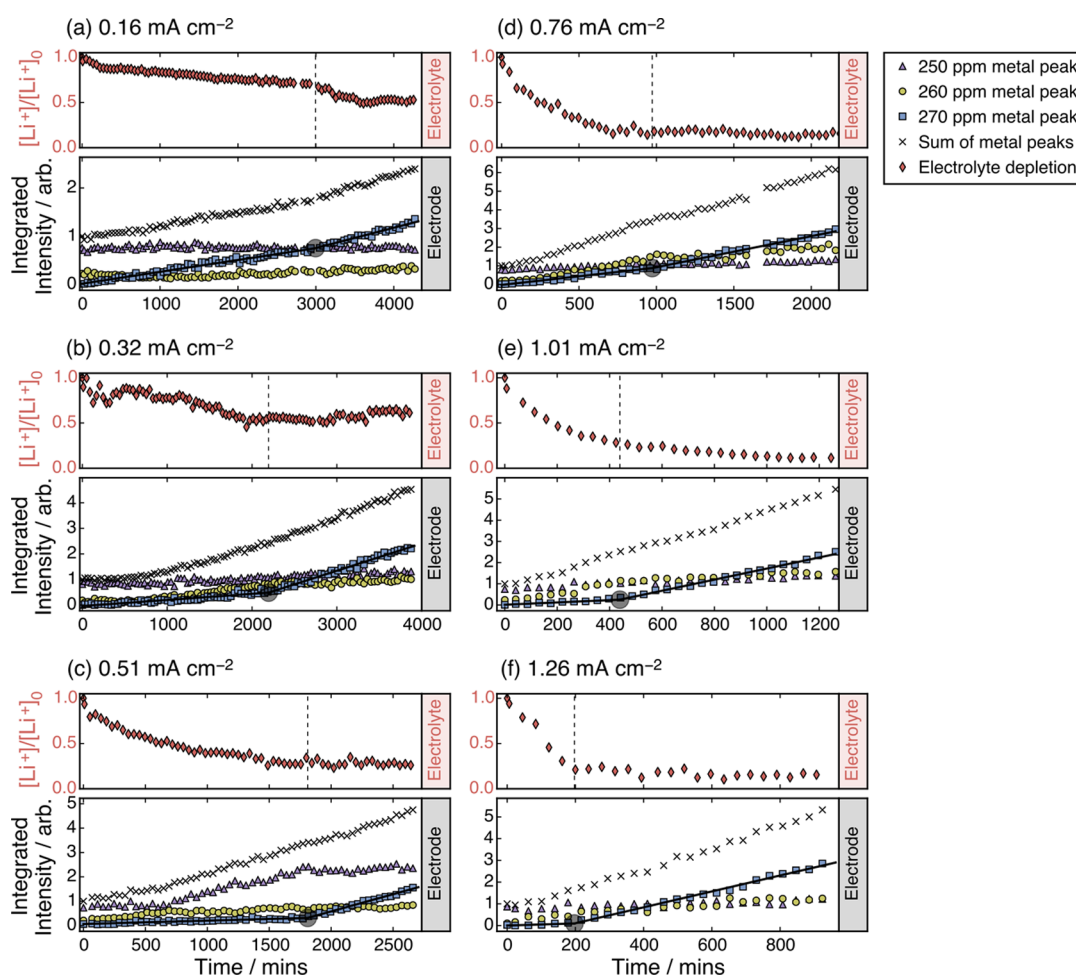

Figure 3. Plots showing changes in the electrolyte concentration near the top electrode (top plot of each pair) and the integrated intensity of the metal peaks (bottom plot of each pair) in the chemical shift images. The metal signal from the top electrode is deconvoluted into three peaks, at 250 ppm for Li bulk metal, 260 ppm for mossy structures, and 270 ppm for dendritic structures, with each series normalized to the sum of the integrated area of the peaks at $t = 0$. The integrated intensity of the peak at 270 ppm was fit to two straight lines for the points above and below the discontinuity in the slopes, with the intersection of those lines circled in each plot and indicated with a dashed vertical line in the electrolyte plot.

shows peaks for the Li metal electrodes at the top (right) and the bottom (left) of the cell, with approximately equal intensities and a chemical shift of ca. 250 ppm. This chemical shift is typical of Li metal oriented perpendicular to $\mathbf{B_0}$,[25,27,29] and is caused by a combination of the Knight shift (261 ppm in ^{7}Li metal[25]) associated with the conducting electrons in the

metal and orientation-dependent bulk magnetic susceptibility effects[25,37] caused by the large paramagnetic susceptibility of Li metal ($\chi_{volume} = 24.1 \times 10^{-6}$).[38] The positions of the electrodes in the metal CSI are seen to overlap with the edges of the electrolyte profile, which is partly due to the low resolution of

the CSIs. The uneven electrode surface also contributes to this effect.

After applying the current for 10.5 h (Figure 2b), the concentration profile noticeably decreases in the vicinity of the negative electrode and increases at the positive electrode. The metal CSI shows a simultaneous increase in intensity over a broad range of shifts centered at ca. 260 ppm at the negative electrode. The linear decrease of the electrolyte signal across the cell continues after the charge has passed for 18.6 h, while the peak at 260 ppm continues to grow in intensity (Figure 2c). However, a new signal at 270 ppm also emerges in the metal image, becoming much more pronounced and extending out appreciably (by 2−3 mm) from the surface of the electrode by the end of charging (Figure 2d). There is a corresponding drop in the Li$^+$ salt concentration in the region that this signal grows into (as shown by the difference with the overlay of the t = 18.6 h data).

The changes in the metal CSI, with peaks emerging downfield from the bulk metal peak, are in stark contrast to the case where the Li deposits smoothly on the surface of the electrode, wherein no change in the metal peak shift or intensity should be observed due to the skin effect, as discussed previously. The peaks at 260 and 270 ppm have been previously assigned to mossy-type and dendritic micro-structures, respectively, on the basis of evidence from studies linking NMR results to SEM observations and susceptibility calculations (the chemical shift relative to the pristine metal peak is attributed to BMS effects resulting from the microstructure morphology and position)[28] and from MRI results linking the chemical shift with the spatial extent of these growths.[29]

These results show that the chosen MRI experiments are able to track changes in both the Li salt concentration profile and the growth of different types of Li microstructure on the surface of the electrode. It can be seen that the concentration of the salt drops in the vicinity of the negative electrode as the Li metal microstructures form, first as a mossy-type structure with a characteristic shift at 260 ppm and then as dendritic structures that extend out appreciably from the surface of the electrode, with a 270 ppm shift. Movies showing similar MRI images acquired as a function of time are provided as Supporting Information for the different currents studied, while plots for the cells charged at the lowest and highest currents are shown in Figures S2 and S3 (SI), respectively. In all of these images, i.e., for currents from 0.16 to 1.26 mA cm^{-2}, two regimes are observed, the first involving moss formation and the second involving dendrite formation.

Simple metrics have been developed in order to compare results from the cells charged at different rates and to correlate the changes in the types of microstructural growth with those occurring in the local electrolyte concentration. For the metal, the signal for the top electrode in the CSI was deconvoluted into peaks at 250, 260, and 270 ppm, approximately corresponding to pristine Li metal, mossy microstructure, and dendritic microstructure, respectively.[28] The time-dependence of the summed integrated area of the 270 ppm peaks was used as the metric for dendrite growth. To quantify the electrolyte depletion, a single position in the electrolyte profile approximately 500 μm from the top electrode was selected and the intensity followed as a function of time. More information about the fitting technique for the metal CSIs and the selection criteria for the electrolyte metric are given in the SI.

Figure 3 depicts the result of the signal quantifications for the dendritic growth and electrolyte depletion as a function of time. Apart from the cell charged at 0.51 mA cm^{-2}, the integral of the metal peak at 250 ppm (purple triangles) remains approx-imately constant throughout charging. This peak is associated with the pristine Li metal environment and any Li$^+$ that deposits smoothly on top of this surface will have the same chemical shift but will not contribute any extra signal intensity due to the rf skin effect.[24,28] The full deconvolutions for the pristine and final CSIs from the 0.51 mA cm^{-2} series are shown in Figure S4 (SI), where the extensive overlap between the peaks at 250 and 260 ppm is apparent, making it difficult to distinguish between the relative growth of these two peaks. Some variation is expected in the types of microstructure growth occurring in the different cells at different cur-rents[18,28,39−41] and therefore in the shift distributions obtained. Nevertheless, the general observation that the intensity of the signal at 250 ppm remains unchanged in the rest of the cells, as expected, suggests that the automatic deconvolution routine is robust.

Although the 250 ppm peak integral remains largely unchanged, the overall ^{7}Li metal signal intensity of the top electrode increases almost immediately from the beginning of charge, in every cell. This increase is seen for the deconvoluted peaks at 260 and 270 ppm, with the exact ratio being slightly different in each cell, presumably because the type of microstructure grown has a slightly different morphology and so a different chemical shift distribution spanning the region from 250 to 280 ppm. Despite these initial differences, at some discrete time in each of the series there is a steep increase in the growth of the fitted 270 ppm peak intensity and a simultaneous halt in the growth of the other peaks. We surmise that this marks a switch from the growth of mossy to dendritic structures. This time also correlates with an increase in the spatial extent of the Li metal growth, observed in the metal CSIs (see, for example, Figure 2c,d), again consistent with the onset of dendrite growth, although estimates based on this metric are less robust. The intersection (circular marker) of lines fit to the data points in Figure 3, above and below this discontinuity, gives an accurate and robust estimate of the time when the first dendrites grow in each of the cells. The predominant growth of the 270 ppm peak after the initiation of dendrite growth indicates that once dendrites form, the deposited Li$^+$ is almost exclusively dendritic. Therefore, dendrites grow at the expense of the more mossy micro-structures (i.e., structures closer to the electrode surface) and continue to grow toward the opposite current collector and into regions where the Li$^+$ ions are not depleted.

The curves showing the electrolyte depletion do, at least at high currents, mirror the changes occurring in the metal CSIs. Initially, there is depletion in the Li$^+$ concentration, which occurs more rapidly in cells charged at higher currents. In each case there is also a discontinuity in the electrolyte concentration curve at or close to the point where dendrite initiation is observed in the metal CSIs, although the nature of this discontinuity is different at high (above 0.51 mA cm^{-2}) as compared to low currents, where it is not as pronounced. One significant difference is that at high currents the Li$^+$ concentration depletes to less than 20% of its starting concentration by the time dendrites start to grow, whereas at low currents there is still a large Li$^+$ concentration close to the electrode. Note that some of this residual Li$^+$ concentration may result from inhomogeneities over the cross section of the

cell, for example, due to the Li microstructure growth, which are not captured in this *z*-projection image. Full 3D imaging would be needed to observe local depletion in the electrolyte, but this is currently infeasible due to the poor signal-to-noise ratio.

The estimates of the dendrite initiation times from the metal CSIs were compared with the time at which the electrolyte depletion is predicted by the Sand's time theory according to eq 2 (Figure 4). Above charging currents of 0.51 mA cm^{-2} there is
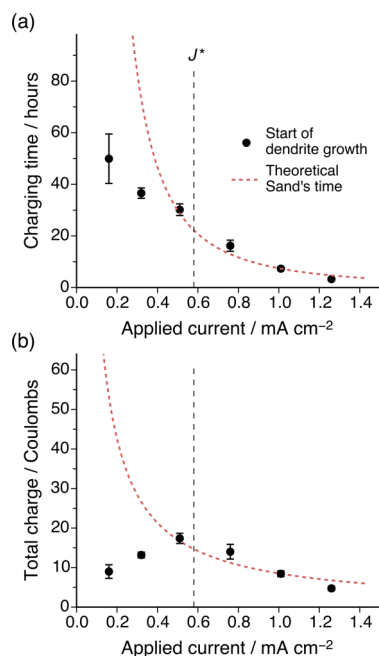

Figure 4. (a) Plot of the theoretical Sand's time and the initiation time of dendrite growth measured experimentally from the discontinuity in the 270 ppm metal peak and (b) the same data, plotted against the total charge applied. Error bars on the experimental values are calculated from the standard error of the fitted lines shown in Figure 3 and their crossing point, with the greater error on the 0.16 mA cm^{-2} data point due to the lines being of similar gradient.

a good agreement with the theoretical prediction, especially considering that there are no adjustable parameters (Figure 4a). At lower currents, dendrite growth is initiated long before the theoretical Sand's time, even when experimental error is accounted for. This is also the region where the Chazalviel model is not explicit about the nature of the growth mechanism. The deviation from the theoretical value of Sand's time is significant and the initiation of dendrite growth does not follow the J^{-2} dependence of the theoretical Sand's time at low currents. This deviation is further amplified when comparing the total charge applied to each cell (i.e., charge = current applied × time) at the times indicated (Figure 4b). On this scale, it is clear that experimentally we observe a maximum in the dendrite-free charging capacity of the cell at intermediate currents around 0.51 mA cm^{-2}. In cells charged above this value, the onset of dendrite growth correlates reasonably well with the theoretical and experimentally observed time at which the electrolyte is depleted at the surface of the negative electrode, suggesting that this is the dominant mechanism triggering dendrite growth at high currents. This trend also agrees well with the qualitative results from the experimentally observed electrolyte depletion in Figure 3.

At low currents, the experimentally determined onset of dendrite growth deviates not only from the theoretical Sand's time values but also from the overall prediction from the theory that at lower currents a higher charge should pass before dendrites start to grow in the cell. This behavior is a strong indication that there is a second mechanism for the initiation of dendrite growth that dominates at low currents and is not directly related to the depletion of the ions in the electrolyte due to limited mass transfer. However, we cannot exclude the possibility that the electrolyte depletes locally in the low current regime caused by, for example, very dense moss formation or thick SEI formation and that this may be the cause of the transition from the mossy to the dendritic growth regime.

The distinct shift from microstructural to dendrite growth would seem to preclude mechanisms for dendrite growth that are dependent on the initial conditions in the cell, such as the roughness of the electrode surface or the stack pressure. However, both of these effects are likely to play a role in the initiation of moss growth. The lack of any separator between the electrodes, and therefore no applied pressure in the cell design used, may be particularly significant in explaining why microstructure growth is observed from the beginning of charge.[28] The SEI must play a role in both moss and dendrite formation because it hinders Li mobility on the Li anode surface. The effective diffusion coefficient of the ions through the SEI is also noticeably lower than in the electrolyte region. Furthermore, it creates hot spots, where the SEI is thinner and ion transport is faster.[42] Once a dendrite starts to grow, new Li is plated. The new Li structure will have a thinner SEI on it and the original SEI film must be disrupted. Li plating will likely then occur preferentially on or near the new growth region due to the higher effective current density at the site of growth. It is possible that the initial moss formation is a consequence of SEI inhomogeneity that leads to nonuniform deposition and therefore local volume changes at the surface of the electrode that can crack the SEI layer and promote microstructure growth.[23] The dendrites then form, at least at high current rates, under control of the electric field and effects related to salt depletion.

The Barton and Bockris model predicts that at a threshold overpotential, the electric field at the tips of existing protrusions promotes spherical diffusion, leading to the initiation of dendrite growth over moss.[11] It is possible that this condition is reached in the low current cells before the electrolyte is depleted, causing the switch from mossy to dendritic growth. The overpotential at the negative electrode was not measured; doing so would require a new cell design incorporating a reference electrode. However, the electrochemistry (see Figure S7, SI) does show that in all but the cell charged at 1.01 mA cm^{-2} there is a gradual increase in the potential difference across the cell leading up to the start of dendrite growth. Of note, in all the cells, we observe a noticeable drop in the cell potential shortly before the MRI-measured onset of dendrite formation, the slight time lag presumably associated with the sensitivity of the CSI experiment to the start of dendrite growth. This drop is particularly pronounced in the intermediate current regime, in which the potential drops steadily after the onset of dendrite formation, possibly caused by the growth of the dendrites toward the opposite current collector.

It appears that, at least in a standard Li ion electrolyte, the eventual growth of lithium dendrites on the Li metal anode is inevitable and will occur regardless of the charge rates.

Additives may, however, play a role in altering the quality of the SEI and thus the Li-dendrite mechanisms. These mechanisms will be explored in future studies.

4. CONCLUSIONS

MRI presents unique opportunities to probe local changes in both solid and liquid phases, making it a particularly valuable methodology with which to study battery chemistry that is governed by changes occurring in different phases. For example, and as illustrated here, such studies can have a great impact on the understanding of the important factors governing dendrite growth in lithium metal batteries.

Chemical shift imaging is a particularly sensitive method for detecting microstructural ^{7}Li growth in situ, with the chemical shift offering sufficient resolution between structures of different morphology even when the spatial resolution is not sufficient to observe the microscopic growth directly. Our results show unequivocally that Li microstructure grows from the start of charge in cells charged at every current used. We show that there are separate conditions for runaway dendrite growth than there are for the initial microstructure growth. A robust analysis of the ^{7}Li CSIs can be performed that can differentiate between the two and extract with relative accuracy the onset time of dendrite growth. At high currents greater than the critical current, dendrite growth is triggered at times near the Sand's time, with a corresponding Li$^+$ ion depletion observed in the ^{7}Li electrolyte images. This observation suggests that limited mass transport is the dominant mechanism governing dendrite onset in this regime. At low currents, electrolyte depletion is not predicted, nor observed experimentally, but dendrite growth is clearly observed. This suggests that a secondary mechanism exists to initiate dendrite growth in the low current regime. The nature and nonuniformity of the SEI could be the cause of such differences, but further work would be required to test this hypothesis.

The experimental and analytical protocols established in this work allow for a reliable and robust estimate of the initiation time of dendrite growth in battery systems and for these changes to be correlated to those occurring in the electrolyte concentration profile. Future work will focus on gaining further insights into the impact of SEI formation, by studying the effects of different electrolytes and additives, and into the role of ionic liquids, where macroscopic concentration gradients are not observed. The methodology is also relevant to modern Li ion (and Na ion) battery anode materials, where dendrite growth or Li (Na) plating is still problematic at high current densities.

■ ASSOCIATED CONTENT

ⓢ Supporting Information

The Supporting Information is available free of charge on the ACS Publications website at DOI: 10.1021/jacs.5b09385.

> Pulse sequences, results for the cells charged at 0.16 and 1.26 mA cm^{-2}, descriptions and examples of the CSI deconvolution and quantification of the electrolyte depletion, and the electrochemistry for all of the cells studied (PDF)
> Movie showing MRI images acquired as a function of time for the cell charged at 0.16 mA cm^{-2} (MOV)
> Movie showing MRI images acquired as a function of time for the cell charged at 0.32 mA cm^{-2} (MOV)

> Movie showing MRI images acquired as a function of time for the cell charged at 0.51 mA cm^{-2} (MOV)
> Movie showing MRI images acquired as a function of time for the cell charged at 0.76 mA cm^{-2} (MOV)
> Movie showing MRI images acquired as a function of time for the cell charged at 1.01 mA cm^{-2} (MOV)
> Movie showing MRI images acquired as a function of time for the cell charged at 1.26 mA cm^{-2} (MOV)

■ AUTHOR INFORMATION

Corresponding Authors
*alexej.jerschow@nyu.edu
*cpg27@cam.ac.uk

Author Contributions
H.J.C. and A.J.I. contributed equally to this work.

Notes
The authors declare no competing financial interest.

■ REFERENCES

(1) Rosso, M.; Brissot, C.; Teyssot, A.; Dolle, M.; Sannier, L.; Tarascon, J. M.; Bouchet, R.; Lascaud, S. *Electrochim. Acta* **2006**, *51*, 5334−5340.
(2) Aurbach, D.; Zinigrad, E.; Cohen, Y.; Teller, H. *Solid State Ionics* **2002**, *148*, 405−416.
(3) Schweikert, N.; Hofmann, A.; Schulz, M.; Scheuermann, M.; Boles, S. T.; Hanemann, T.; Hahn, H.; Indris, S. *J. Power Sources* **2013**, *228*, 237−243.
(4) Mayers, M. Z.; Kaminski, J. W.; Miller, T. F. *J. Phys. Chem. C* **2012**, *116*, 26214−26221.
(5) Ding, F.; Xu, W.; Graff, G. L.; Zhang, J.; Sushko, M. L.; Chen, X.; Shao, Y.; Engelhard, M. H.; Nie, Z.; Xiao, J.; Liu, X.; Sushko, P. V.; Liu, J.; Zhang, J. G. *J. Am. Chem. Soc.* **2013**, *135*, 4450−6.
(6) Arora, P.; Zhang, Z. M. *Chem. Rev.* **2004**, *104*, 4419−4462.
(7) Zhang, X. W.; Li, Y. X.; Khan, S. A.; Fedkiw, P. S. *J. Electrochem. Soc.* **2004**, *151*, A1257−A1263.
(8) Kanamura, K.; Shiraishi, S.; Takehara, Z. *J. Electrochem. Soc.* **1996**, *143*, 2187−2197.
(9) Eastwood, D. S.; Bayley, P. M.; Chang, H. J.; Taiwo, O. O.; Vila-Comamala, J.; Brett, D. J.; Rau, C.; Withers, P. J.; Shearing, P. R.; Grey, C. P.; Lee, P. D. *Chem. Commun.* **2015**, *51*, 266−268.
(10) Li, Z.; Huang, J.; Yann Liaw, B.; Metzler, V.; Zhang, J. *J. Power Sources* **2014**, *254*, 168−182.
(11) Diggle, J. W.; Despic, A. R.; Bockris, J. O. M. *J. Electrochem. Soc.* **1969**, *116*, 1503−1514.

(12) Barton, J. L.; Bockris, J. O. M. *Proc. R. Soc. London, Ser. A* **1962**, *268*, 485.

(13) Witten, T.; Sander, L. *Phys. Rev. Lett.* **1981**, *47*, 1400−1403.

(14) Magan, R. V.; Sureshkumar, R.; Lin, B. *J. Phys. Chem. B* **2003**, *107*, 10513−10520.

(15) Chazalviel, J.-N. *Phys. Rev. A* **1990**, *42*, 7355.

(16) Meakin, P. *Phys. Rev. Lett.* **1983**, *51*, 1119.

(17) Voss, R. F.; Tomikiewicz, M. *J. Electrochem. Soc.* **1985**, *132*, 371−375.

(18) Brissot, C.; Rosso, M.; Chazalviel, J.-N.; Lascaud, S. *J. Electrochem. Soc.* **1999**, *146*, 4393−4400.

(19) Brissot, C.; Rosso, M.; Chazalviel, J. N.; Lascaud, S. *J. Power Sources* **2001**, *94*, 212−218.

(20) Park, H. E.; Hong, C. H.; Yoon, W. Y. *J. Power Sources* **2008**, *178*, 765−768.

(21) Aurbach, D. *J. Power Sources* **2000**, *89*, 206−218.

(22) Mogi, R.; Inaba, M.; Jeong, S.-K.; Iriyama, Y.; Abe, T.; Ogumi, Z. *J. Electrochem. Soc.* **2002**, *149*, A1578.

(23) Cohen, Y. S.; Cohen, Y.; Aurbach, D. *J. Phys. Chem. B* **2000**, *104*, 12282−12291.

(24) Bhattacharyya, R.; Key, B.; Chen, H.; Best, A. S.; Hollenkamp, A. F.; Grey, C. P. *Nat. Mater.* **2010**, *9*, 504−510.

(25) Ilott, A. J.; Chandrashekar, S.; Klockner, A.; Chang, H. J.; Trease, N. M.; Grey, C. P.; Greengard, L.; Jerschow, A. *J. Magn. Reson.* **2014**, *245*, 143−149.

(26) Zhou, L.; Leskes, M.; Ilott, A. J.; Trease, N. M.; Grey, C. P. *J. Magn. Reson.* **2013**, *234*, 44−57.

(27) Trease, N. M.; Zhou, L.; Chang, H. J.; Zhu, B. Y.; Grey, C. P. *Solid State Nucl. Magn. Reson.* **2012**, *42*, 62−70.

(28) Chang, H. J.; Trease, N. M.; Ilott, A. J.; Zeng, D.; Du, L. S.; Jerschow, A.; Grey, C. P. *J. Phys. Chem. C* **2015**, *119*, 16443−16451.

(29) Chandrashekar, S.; Trease, N. M.; Chang, H. J.; Du, L.-S.; Grey, C. P.; Jerschow, A. *Nat. Mater.* **2012**, *11*, 311−315.

(30) Klett, M.; Giesecke, M.; Nyman, A.; Hallberg, F.; Lindstrom, R. W.; Lindbergh, G.; Furo, I. *J. Am. Chem. Soc.* **2012**, *134*, 14654−7.

(31) Klamor, S.; Zick, K.; Oerther, T.; Schappacher, F. M.; Winter, M.; Brunklaus, G. *Phys. Chem. Chem. Phys.* **2015**, *17*, 4458−4465.

(32) Nyman, A.; Behm, M.; Lindbergh, G. *Electrochim. Acta* **2008**, *53*, 6356−6365.

(33) Gutowsky, H. S.; McGarvey, B. R. *J. Chem. Phys.* **1952**, *20*, 1472−1477.

(34) Marques, J. P.; Bowtell, R. *Concepts Magn. Reson., Part B* **2005**, *25B*, 65−78.

(35) Britton, M. M.; Bayley, P. M.; Howlett, P. C.; Davenport, A. J.; Forsyth, M. *J. Phys. Chem. Lett.* **2013**, *4*, 3019−3023.

(36) Britton, M. M. *ChemPhysChem* **2014**, *15*, 1731−1736.

(37) Kubo, A.; Spaniol, T. P.; Terao, T. *J. Magn. Reson.* **1998**, *133*, 330−340.

(38) Gugan, D. *Phys. Rev. B* **1997**, *56*, 7759.

(39) Sano, H.; Sakaebe, H.; Senoh, H.; Matsumoto, H. *J. Electrochem. Soc.* **2014**, *161*, A1236−A1240.

(40) Gireaud, L.; Grugeon, S.; Laruelle, S.; Yrieix, B.; Tarascon, J. M. *Electrochem. Commun.* **2006**, *8*, 1639−1649.

(41) Aurbach, D.; Zinigrad, E.; Teller, H.; Dan, P. *J. Electrochem. Soc.* **2000**, *147*, 1274−1279.

(42) Peled, E. *J. Electrochem. Soc.* **1979**, *126*, 2047−2051.